



Cite this: *Nanoscale Horiz.*, 2020, 5, 1332

Received 5th May 2020,
Accepted 23rd July 2020

DOI: 10.1039/d0nh00263a

rsc.li/nanoscale-horizons

Effect of alkaline earth metal chloride additives BCl_2 ($\text{B} = \text{Mg, Ca, Sr and Ba}$) on the photovoltaic performance of FAPbI_3 based perovskite solar cells[†]

Mei Lyu, Do-Kyoung Lee and Nam-Gyu Park  *

Additive engineering is known to be an effective method for inducing a simultaneous effect of enlarging the grain size and surface passivation. As compared to the monovalent halides frequently used as additives, divalent halides are relatively less investigated in the role of additives. In this work, we report effects of alkaline earth metal halides BCl_2 ($\text{B} = \text{Mg, Ca, Sr, Ba}$) as additives on the opto-electronic properties and photovoltaic performance of FAPbI_3 based perovskite solar cells (PSCs). A significant improvement in power conversion efficiency (PCE) from 17.27% to 21.11% is observed by MgCl_2 addition in the FAPbI_3 precursor solution, while a marginal increment for CaCl_2 or BaCl_2 and a negative effect for SrCl_2 is observed. The lattice constant of cubic FAPbI_3 is hardly changed by additives, while the crystallinity is improved by MgCl_2 . The carrier lifetime increases from 40 ns to 287 ns and the trap density is reduced from $1.08 \times 10^{16} \text{ cm}^{-3}$ to $3.19 \times 10^{15} \text{ cm}^{-3}$ by addition of 5 mol% MgCl_2 , which is responsible for the enhancement in photovoltaic parameters. The steady-state PCE of the PSC with the MgCl_2 -additive-treated FAPbI_3 measured under continuous illumination at the maximum power point remains unchanged for 1500 s.

Introduction

Since the report of a 9.7% efficient and 500 h stable solid-state perovskite solar cell (PSC) in 2012,¹ developed to solve the instability of methylammonium lead iodide (MAPbI_3) in a liquid electrolyte,^{2,3} a swift surge in perovskite photovoltaics led to a certified power conversion efficiency (PCE) of 25.2% in 2019.⁴ The inherently excellent opto-electronic properties of organic lead halide perovskites^{5–7} are responsible for the superb photovoltaic performance, which might be better than the well-known thin film solar cell materials such as $\text{Cu}(\text{In}_{1-x}\text{Ga}_x)\text{Se}_2$, multi-crystalline Si and CdTe because of higher PCE. Among the

New concepts

Formamidinium lead iodide (FAPbI_3) perovskite is known to be an ideal material among the studied compositions in terms of optical bandgap. The precursor solution is suggested to include an additive – normally, the monovalent cationic chlorides, such as MACl or CsCl , are frequently used as additives – to improve the photovoltaic performance of FAPbI_3 perovskite solar cells (PSCs). However, a change in bandgap is expected because MA or Cs cations can replace the FA cations. Thus, it is required to keep the bandgap of FAPbI_3 even after modification by additive engineering. As compared to the monovalent halides, no systematic investigation on the role of divalent halides has been reported in FAPbI_3 based PSCs. In this work, we first report the effects of alkaline earth metal halide BCl_2 ($\text{B} = \text{Mg, Ca, Sr, Ba}$) additives on the opto-electronic properties and photovoltaic performance of FAPbI_3 based PSCs. We have found that the addition of MgCl_2 improves the power conversion efficiency significantly due to a large increase in carrier lifetime and a significant reduction in trap density. In addition, no change in bandgap is observed because of the higher oxidation state and much smaller ionic radius of Mg^{2+} than FA and Pb cations.

studied compositions for PSCs, FAPbI_3 ($\text{FA} = \text{formamidinium}$) has been regarded as an ideal perovskite because of suitable bandgap (~ 1.47 eV) and no structural phase transition at the operating temperature.⁸ However, the photoactive FAPbI_3 is known to be in the high-temperature stabilized α phase, and tends to undergo phase transition from α to photo-inactive δ phase at ambient temperature.⁹ It was first reported that a substitution of a certain amount of FA cations with Cs cations can stabilize the α phase at ambient temperature.¹⁰ In general, substitution with smaller monovalent cations (Cs^+ , Rb^+ or MA) and/or halide anion (Br^-) was found to stabilize the α phase of FAPbI_3 thermodynamically.^{11–14} Thus, these cations can be referred to as “stabilizers” in FAPbI_3 .¹²

The stabilizers can be incorporated compositionally by stoichiometrically mixing FA with a certain amount of stabilizer, which is called “compositional engineering”. The incorporation of stabilizer is also possible by “additive engineering” in which an adequate amount of additive is mixed with FAPbI_3 precursor. The difference between compositional engineering

School of Chemical Engineering, Sungkyunkwan University, Suwon 16419, Korea.
E-mail: npark@skku.edu

† Electronic supplementary information (ESI) available. See DOI: 10.1039/d0nh00263a

and additive engineering is that additive engineering is a non stoichiometric approach and elements that may not be involved in the composition can be used as additives. Additive engineering has been found to be also beneficial for both surface passivation and growth of grain size.¹⁵ It is well-known that addition of MACl additive in a perovskite precursor solution shows a positive effect on the photovoltaic performance of FAPbI₃ based PSCs.^{16–18} Although it has been argued whether or not chloride is incorporated in iodide sites, it is widely accepted that chloride plays an important role in enlarging the grain size and improving crystallinity.¹⁹ Since there is a positive effect of chloride in additives, we have been motivated to systematically investigate the effect of divalent alkaline earth metal chlorides, BCl₂ (B = Mg, Ca, Sr and Ba), on the photovoltaic performance and stability of FAPbI₃ based PSCs. Since the divalent cations in BCl₂ are smaller in ionic radius (Mg²⁺ = 72 pm, Ca²⁺ = 100 pm, Sr²⁺ = 118 pm, and Ba²⁺ = 135 pm) and have higher formal charge than the FA cation, the surface passivation effect is expected rather than the substitution effect. In addition, the chloride content of BCl₂ is twice that of monovalent chloride when the same quantity is dissolved in the precursor solution, which may also affect the opto-electronic properties of the PSCs. To the best of our knowledge, no systematic studies have been reported on the additive engineering of FAPbI₃ with BCl₂.

Here, we report on the effects of BCl₂ additives on the photovoltaic parameters and opto-electronic properties of the FAPbI₃ based PSCs. The additive BCl₂ is mixed with a pre-synthesized FAPbI₃ powder,²⁰ where the concentration of BCl₂, [BCl₂], is varied with respect to [FAPbI₃]. Among the studied additives, MgCl₂ is found to improve the photovoltaic performance and stability. Crystal structure, film morphology, band alignment and carrier lifetime are comparatively investigated to understand the basis for the improvement. A pristine FAPbI₃ device shows a PCE of 17.27% which is significantly improved to 21.11% by addition of MgCl₂ in the FAPbI₃ precursor solution.

Results and discussion

Effect of BCl₂ (B = Mg, Ca, Sr and Ba) on the opto-electronic properties of FAPbI₃ and photovoltaic performance

The perovskite precursor solutions are prepared by mixing the pre-synthesized FAPbI₃ powder (yellow δ phase) with BCl₂ with

different molar ratios (see Experimental details). In order to investigate how the metal precursor additives change the reactivity of the perovskite precursors, UV-vis absorption spectroscopy of the precursor solution is studied. Fig. S1 (ESI[†]) shows that the absorption band around 310 nm is due to the iodoplumbate (probably PbI₂(DMF)_x(DMSO)_{4-x} species), where peak intensity is higher for the MgCl₂ additive than for other additives. A strong absorption is indicative of an increase in iodoplumbate concentration and thereby an improvement of photovoltaic performance.²¹ Another weak absorption peak at around 380 nm (inset in Fig. S1, ESI[†]) is related to PbI₃⁻.²² This peak is also relatively intense for the MgCl₂ additive compared to other additives. When considering that two characteristic peaks in the precursor solution affect the photovoltaic performance, MgCl₂ additive is expected to be better in performance than other additives, which will be further evaluated. Fig. 1 shows a schematic illustration of perovskite deposition, where the precursor solution with and without additive is spin-coated on a SnO₂ coated FTO (fluorine-doped tin oxide) substrate. To control the crystal growth, an intermediate is formed by dripping diethyl ether during the spin-coating procedure.²³ The thickness of the 150 °C-annealed perovskite film is about 440 nm as confirmed from cross-sectional scanning electron microscopy (SEM) (images not shown).

The effects of the concentration of the additives on the photovoltaic parameters are investigated. As shown in Fig. S2 (ESI[†]), the photovoltaic parameters are strongly dependent on the additive concentration (note that the final concentration may be different because the solution was filtered prior to use), from which an optimal concentration is determined to be 5 mol% for MgCl₂, 1 mol% for CaCl₂ and 9 mol% for BaCl₂. In contrast to the Mg, Ca and Ba cases, the addition of SrCl₂ additive lowers the photovoltaic performance. Despite the negative effect of SrCl₂, 10 mol% shows better performance among the tested concentrations from 5 mol% to 15 mol%. Fig. 2 shows the statistical short-circuit photocurrent density (J_{sc}), open-circuit voltage (V_{oc}), fill factor (FF) and power conversion efficiency (PCE) for the optimal concentration of BCl₂ additives. Unlike the BI₂ additives doped in MAPbI₃,^{24,25} 5 mol% MgCl₂ improves substantially V_{oc} and FF, while a negligible or slight enhancement is observed for CaCl₂ and BaCl₂. Mean values are listed in Table 1, where the average PCE estimated from the

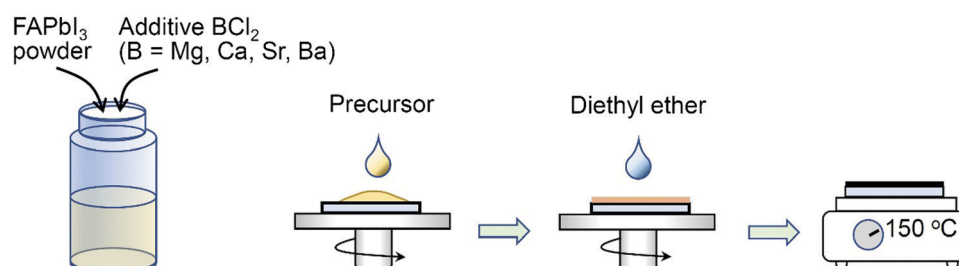


Fig. 1 A schematic illustration of the perovskite deposition procedure. The precursor solution was prepared by mixing the pre-synthesized FAPbI₃ powder with BCl₂ additive (B = Mg, Ca, Sr and Ba), which was spin-coated. Diethyl ether was dripped for 20 s after rotating the substrate. The film was annealed at 150 °C in an air atmosphere.

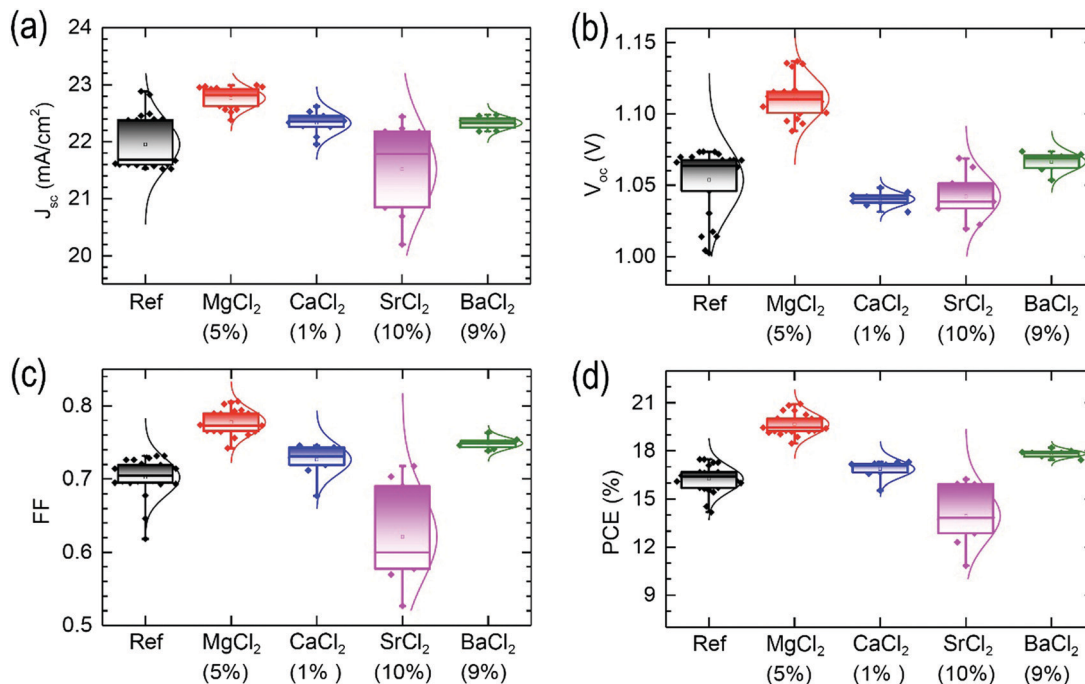


Fig. 2 Statistical photovoltaic parameters of (a) J_{sc} , (b) V_{oc} , (c) FF and (d) PCE measured at reverse scan for the BCl₂ additives (B = Mg, Ca, Sr and Ba). Values in parentheses are the optimal mol% of the additive with respect to FAPbI₃.

Table 1 Mean photovoltaic parameters of PSCs employing FAPbI₃ perovskite films with and without (Ref) BCl₂ additives (B = Mg, Ca, Sr and Ba). FS and RS stand for forward scan and reverse scan, respectively

Additive (mol%)	J_{sc} (mA cm ⁻²)	V_{oc} (V)	FF	PCE (%)
Ref (w/o)	FS: 21.84 ± 0.42 RS: 21.97 ± 0.68	FS: 1.07 ± 0.01 RS: 1.05 ± 0.03	FS: 0.72 ± 0.03 RS: 0.71 ± 0.03	FS: 16.66 ± 1.06 RS: 16.38 ± 1.02
MgCl ₂ (5%)	FS: 22.72 ± 0.41 RS: 22.76 ± 0.31	FS: 1.11 ± 0.02 RS: 1.11 ± 0.02	FS: 0.77 ± 0.02 RS: 0.78 ± 0.03	FS: 19.36 ± 0.98 RS: 19.67 ± 1.23
CaCl ₂ (1%)	FS: 22.37 ± 0.33 RS: 22.11 ± 0.33	FS: 1.05 ± 0.01 RS: 1.04 ± 0.01	FS: 0.72 ± 0.04 RS: 0.70 ± 0.03	FS: 16.86 ± 0.89 RS: 16.09 ± 0.88
SrCl ₂ (10%)	FS: 21.57 ± 1.12 RS: 21.52 ± 1.12	FS: 1.04 ± 0.03 RS: 1.04 ± 0.02	FS: 0.57 ± 0.13 RS: 0.62 ± 0.10	FS: 12.75 ± 3.70 RS: 13.95 ± 2.69
BaCl ₂ (9%)	FS: 22.21 ± 0.43 RS: 22.33 ± 0.15	FS: 1.07 ± 0.01 RS: 1.07 ± 0.01	FS: 0.75 ± 0.01 RS: 0.75 ± 0.01	FS: 17.66 ± 0.40 RS: 17.82 ± 0.39

reverse scanned parameters is improved from 16.39% to 19.66% by MgCl₂ addition. A large improvement in V_{oc} and FF implies that recombination might be reduced by the MgCl₂ additive. In our study, bulk doping in FAPbI₃ with SrCl₂ shows a negative effect leading to deterioration of the photovoltaic performance, which is in contrast to the previous work reporting an improved PCE by the 10–30% doping with SrCl₂ in MAPbI₃ and even the 2% doping with SrI₂ in CsPbI₃.^{26,27}

Surface morphology is not significantly altered by MgCl₂, while CaCl₂, SrCl₂ and BaCl₂ change the surface morphology of FAPbI₃ (Fig. 3(a–e)). Cross-sectional SEM images confirm that MgCl₂ results in a pinhole-free interface between SnO₂ and perovskite, whereas large pinholes are formed at the interface for the pristine FAPbI₃. This indicates that the MgCl₂ additive supports an underlying conformal growth of perovskite on the substrate. The MgCl₂ additive is expected to contribute to the enlargement of the grain size of FAPbI₃ perovskite due to

the higher coordination interaction between FA⁺ and Mg²⁺ than those of FA⁺ and Pb²⁺.^{28,29} and/or retarded crystallization kinetics.³⁰ The higher J_{sc} obtained from the MgCl₂ additive is thus probably due to better charge collection owing to the pinhole-free interface. In addition, the crystallinity of α phase FAPbI₃ is improved in the presence of MgCl₂ as confirmed from the X-ray diffraction (XRD) pattern in Fig. 3(f), which might be associated with higher V_{oc} and FF because of the long-range ordering of FAPbI₃ and thereby less defects. On the other hand, the addition of CaCl₂, SrCl₂ and BaCl₂ cannot fully convert the δ phase to α phase because the δ phase is still present in the annealed film (Fig. 3(g)). Moreover, the CaCl₂ additive increases the unreacted PbI₂ peak, implying a strong interaction between CaCl₂ and PbI₂ in the precursor solution. Although the ionic radius of Sr²⁺ (118 pm) is similar to that of Pb²⁺ (119 pm), Sr²⁺ is not likely to replace Pb²⁺ because unreacted SrCl₂ exists in the annealed film as shown in the XRD peak at around 12.8° in Fig. 3(g) and the lattice constant of cubic FAPbI₃³¹ is unchanged by SrCl₂ due to no peak shift in the (100) reflection at $2\theta = 13.94^\circ$.

Energy dispersive X-ray spectroscopy (EDS) is carried out to investigate the presence of BCl₂ in the annealed FAPbI₃ film. For the MgCl₂ case in Fig. 4(a), neither Mg nor Cl is detected on the film surface. Similarly, Ca and Cl are not detected on the film surface for FAPbI₃ with CaCl₂ additive (Fig. 4(b)). However, for the SrCl₂ and BaCl₂ cases, Sr, Ba and Cl elements are detected with an atomic ratio of Sr:Cl or Ba:Cl = 1:2 (Fig. 4(c) and (d)). No detection of MgCl₂ and CaCl₂ is probably due to the relatively lower concentration as compared to SrCl₂ and BaCl₂. The ratio of I to Pb is found to be almost 3 (atomic ratio I:Pb = 18.86:6.16) for the MgCl₂ case, which is indicative of stoichiometric formation of FAPbI₃. On the other hand, iodide-rich

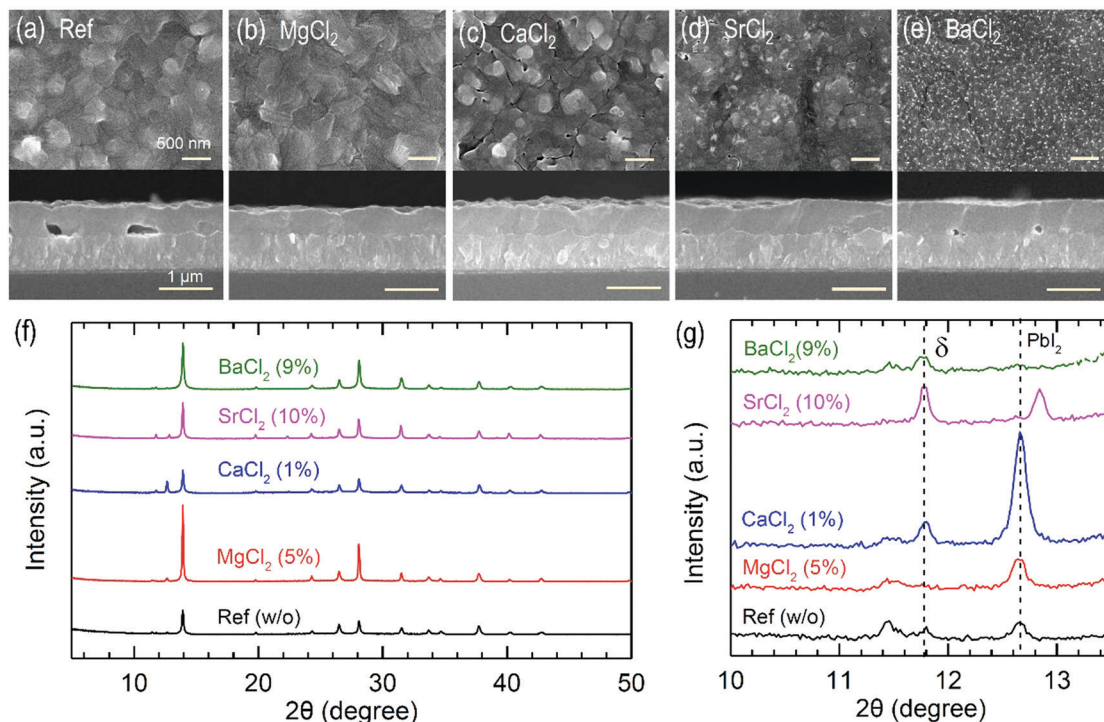


Fig. 3 (a–e) Top-view and cross-sectional scanning electron microscope (SEM) images and (f, g) X-ray diffraction patterns of FAPbI₃ films with and without (Ref) additives of MgCl₂, CaCl₂, SrCl₂ and BaCl₂.

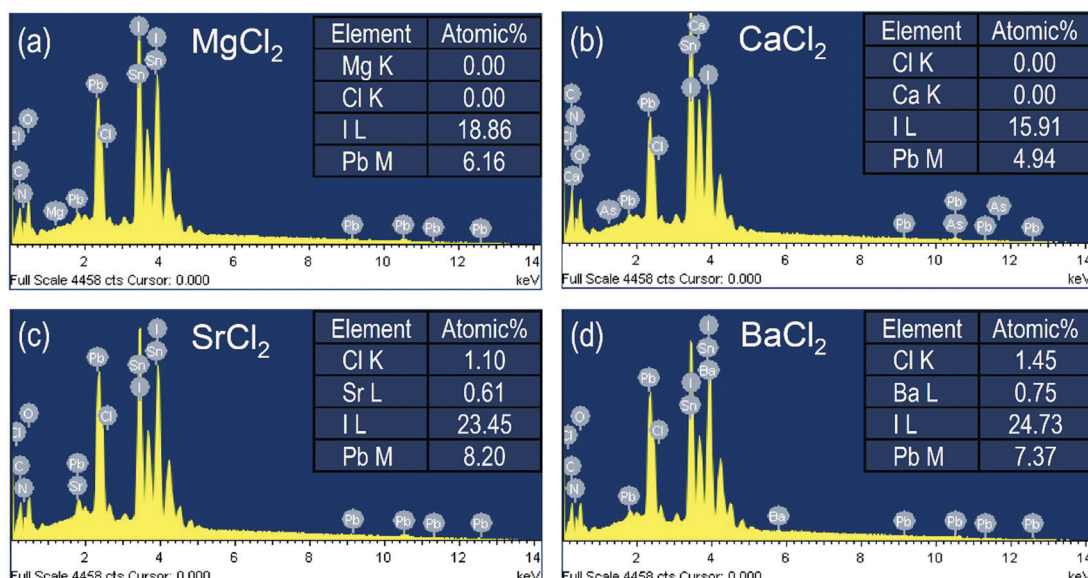


Fig. 4 Energy dispersive X-ray spectroscopy (EDS) of FAPbI₃ films with additive of (a) MgCl₂ (5%), (b) CaCl₂ (1%), (c) SrCl₂ (10%) and (d) BaCl₂ (9%).

(or Pb-deficient) phase is formed for CaCl₂ and BaCl₂ because of the ratio I/Pb = 3.22 (CaCl₂) and 3.35 (BaCl₂). Addition of SrCl₂ results in iodide-deficient (or Pb-rich) phase in the annealed perovskite film. Although excess PbI₂ or organic iodide was reported to passivate the perovskite grain boundary and thereby improve the photovoltaic performance,^{32,33} the stoichiometry of the perovskite was also reported to play an important role in photovoltaic performance and stability because defects can be

minimized by stoichiometric composition.³⁴ Thus, stoichiometric FAPbI₃ formed by MgCl₂ additive is in part responsible for the improved PCE. Since detection of MgCl₂ and CaCl₂ is unavailable by EDS, we further measure surface-sensitive X-ray photoelectron spectroscopy (XPS) to understand the chemical environment of FAPbI₃ films depending on additives.

Fig. 5(a–d) show Mg 1s, Ca 2p, Sr 3d and Ba 3d XPS spectra before and after addition of the additives. The film samples for

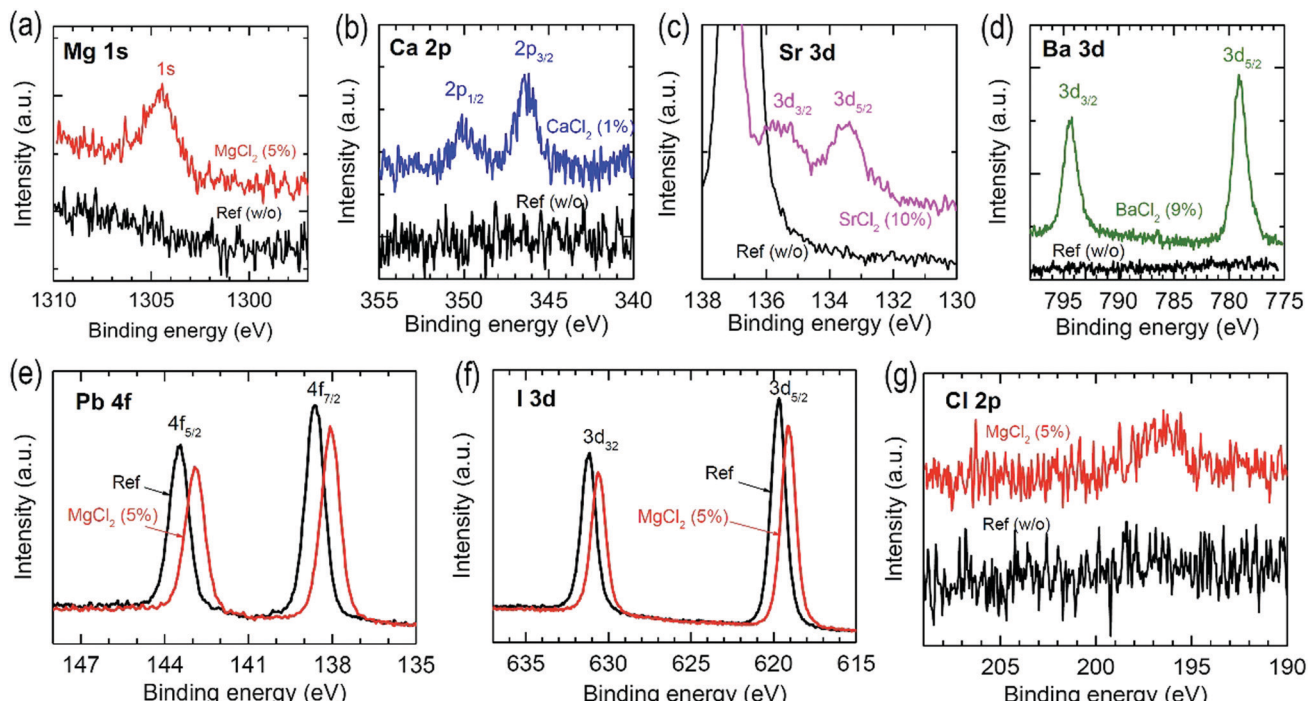


Fig. 5 Mg 1s, Ca 2p, Sr 3d and Ba 3d X-ray photoelectron spectroscopy (XPS) spectra of the annealed FAPbI₃ films with and without additives of (a) MgCl₂, (b) CaCl₂, (c) SrCl₂ and (d) BaCl₂. (e) Pb 4f, (f) I 3d and (g) Cl 2p XPS spectra of the FAPbI₃ films before and after adding the MgCl₂ additive.

XPS measurements were prepared on Si wafers. Mg, Ca, Sr and Ba elements are obviously detected. The detection of Cl from the MgCl₂-treated FAPbI₃ film confirms the existence of MgCl₂ in the film (see Fig. 5(g)). Thus, the additives still exist in the annealed perovskite films. Since addition of MgCl₂ significantly improved the photovoltaic performance among the studied BCl₂ additives, we further investigate Pb 4f and I 3d XPS for the FAPbI₃ films with and without MgCl₂. In Fig. 5(e), the pristine FAPbI₃ film shows two peaks at binding energies of 143.53 eV and 138.63 eV, which correspond to the Pb 4f_{5/2} and 4f_{7/2} core levels, respectively, originated from Pb²⁺ ions.^{35,36} The addition of MgCl₂ in FAPbI₃ shifts the Pb 4f peaks to lower binding energies of 142.93 eV for 4f_{5/2} and 138.08 eV for 4f_{7/2}. Shift to lower binding energy after adding MgCl₂ is also observed from I 3d XPS (Fig. 5(f)), where the 3d_{3/2} peak at 631.13 eV and the 3d_{5/2} peak at 619.68 eV shift to 630.63 eV and 619.13 eV. When considering no change in lattice constant by MgCl₂, Mg or Cl element might not be directly involved in lattice construction. Thus, the shift in binding energy is indicative of a change in chemical environment around Pb and I at the surface. The decrease in binding energy of Pb²⁺ and I⁻ is probably related to an increase in electron density around Pb²⁺ and I⁻.³⁷⁻³⁹ In the case that Mg²⁺ interacts with iodide at the surface, the (Pb-I) bond is more likely to be ionic due to an increased covalency of the adjacent (Mg-I) bond because of the smaller ionic radius of Mg²⁺ (72 pm) than Pb²⁺ (119 pm) according to Fajan's rule.⁴⁰ Thus, the electron density of iodide in the (Mg-I-Pb) interaction is relatively increased as compared to the (Pb-I-Pb) configuration. In addition, the more covalent character of (Mg-I) will donate electrons to Pb, which increases

the electron density of Pb. Chloride in MgCl₂ can also affect the shift of the Pb 4f and the I 3d peaks by donating lone-pair electrons to the perovskite surface. It was reported that post-treatment with SrCl₂ was found to shift the Pb 4f and the I 3d core levels to lower binding energy.⁴¹

Modification of the optical bandgap and band position is studied using UV-vis and ultraviolet photoelectron spectroscopy (UPS). Fig. 6(a) shows the UV-vis spectra of the annealed FAPbI₃ with and without additives. The absorbance is slightly enhanced by the additives, which is attributed to a slight increase in J_{sc} . Despite better absorbance observed from the SrCl₂ case, the lower J_{sc} than the reference device might be related to the presence of unconverted δ phase and/or poor SnO₂/perovskite interface in the aforementioned Fig. 3. The Taue plot obtained from the UV-vis spectral data is shown in Fig. 6(b), where a linear fit in the 1.54–1.57 eV range of photon energy reveals that the optical bandgap (E_g) is determined to be 1.50 eV for MgCl₂ and CaCl₂ and 1.51 eV for SrCl₂ and BaCl₂, which are almost unchanged as compared to the pristine FAPbI₃ (E_g = 1.50 eV). Unaltered E_g is consistent with the invariable lattice constant as observed in XRD. Our result is different from the doping effect on E_g of MAPbI₃ or CsPbI₃, where E_g was influenced by doping due to the substitution effect.⁴²⁻⁴⁵ Valence band (E_{VB}) and conduction band (E_{CB}) positions are determined from UPS using He I photon energy ($h\nu$ = 21.2 eV). In Fig. 6(c), UPS spectra are illustrated, showing the binding energy region of the cut-off energy (E_{cutoff}) and the valence band maximum (VBM). Work function (WF) is determined from $WF = h\nu - E_{cutoff}$ (see Fig. S3 (ESI[†]) for determining E_{cutoff}) and E_{VB} is determined using $E_{VB} = WF + VBM$ (see Fig. S3 (ESI[†]) for determining VBM).⁴⁶ To determine

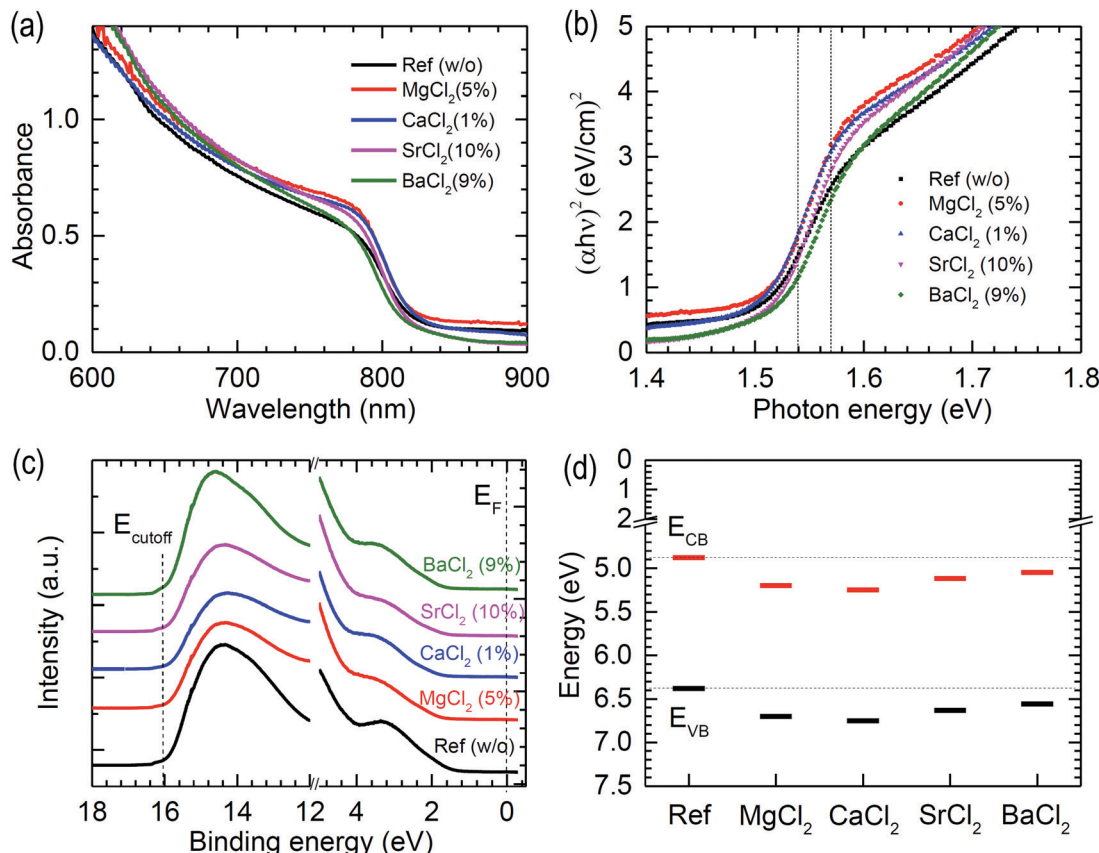


Fig. 6 (a) UV-vis spectra, (b) Tauc plot, (c) ultraviolet photoelectron spectroscopy (UPS) and (d) band (conduction band (CB) and valence band (VB)) positions for the FAPbI₃ films with and without additives. UPS spectra were measured with He I photon energy (21.2 eV).

Table 2 Work function (WF), valence band energy (E_{VB}) and conduction band energy (E_{CB}) estimated from the cut-off energy (E_{cutoff}), valence band maximum (VBM) and optical bandgap (E_g)

Sample	E_{cutoff} (eV)	WF (eV)	VBM (eV)	E_{VB} (eV)	E_g (eV)	E_{CB} (eV)
Ref (w/o)	16.05	5.15	1.23	6.38	1.50	4.88
MgCl ₂ (5%)	16.05	5.15	1.55	6.70	1.50	5.20
CaCl ₂ (1%)	16.00	5.20	1.55	6.75	1.50	5.25
SrCl ₂ (10%)	16.02	5.18	1.45	6.63	1.51	5.12
BaCl ₂ (9%)	16.11	5.09	1.47	6.56	1.51	5.05

VBM, we use a logarithmic scale method.⁴⁷ The estimated values are listed in Table 2 and plotted in Fig. 6(d). E_{VB} is determined to be 6.38 eV for the non-additive pristine FAPbI₃, which is consistent with the reported value obtained from the combined experimental and theoretical data.⁴⁸ Upon addition of additives, WF is almost unchanged, which indicates that the additive might not act as a dopant. Unlike the BI₂ additive in MAPbI₃ perovskite, resulting in up-shift of E_{VB} and E_{CB} ,⁴⁹ E_{VB} is down-shifted by the BCl₂ additives in FAPbI₃ perovskite films. The chloride seems to play a common effect on down-shifting E_{VB} . Since the antibonding-nature E_{VB} for the pristine FAPbI₃ is formed by overlapping the Pb 6s orbital with the I 5p from the viewpoint of molecular orbital theory, the chloride at the surface is likely to lower the E_{VB} because of overlap with a more electronegative Cl 3p orbital.⁵⁰ It was reported that a low concentration of Mg doping

into MAPbI₃ led to down-shift of E_{VB} and more n-type property.⁵¹ Thus, more n-type FAPbI₃ might be induced by addition of MgCl₂.

Effect of MgCl₂ additive on carrier mobility and trap density of FAPbI₃

The improved V_{oc} by MgCl₂ additive in spite of the unchanged E_g underlines that carrier lifetime, associated with trap density, is probably improved. To verify this hypothesis, we measure time-resolved photoluminescence (TRPL) along with steady-state PL. In Fig. 7(a), the PL intensity of the bulk perovskite film is increased by MgCl₂, which is indicative of reduction of non-radiative recombination. Upon contacting the perovskite film with SnO₂, the PL intensity is similarly decreased by 90.4% (pristine) and 89.5% (MgCl₂). Despite a similar degree of PL quenching, a lower J_{sc} for the pristine FAPbI₃ is due to the presence of pinholes at the SnO₂/perovskite interface (see Fig. 3). The TRPL spectrum in Fig. 7(b) is fit with the bi-exponential decay equation, $f(t) = A_1 \exp(-t/\tau_1) + A_2 \exp(-t/\tau_2)$, where τ_1 and τ_2 are time constants and A_1 and A_2 are amplitude.³³ Table 3 lists the fit results of pristine perovskite and perovskite film with MgCl₂ additive on the glass substrate. The addition of MgCl₂ increases τ_1 from 1.9 ns to 3.9 ns and τ_2 from 201.2 ns to 376.5 ns. In addition, the amplitude ratio (A_1/A_2) decreases significantly from 447.9 to 30.3 after addition of MgCl₂. This decrease in A_1/A_2 indicates that the contribution of the

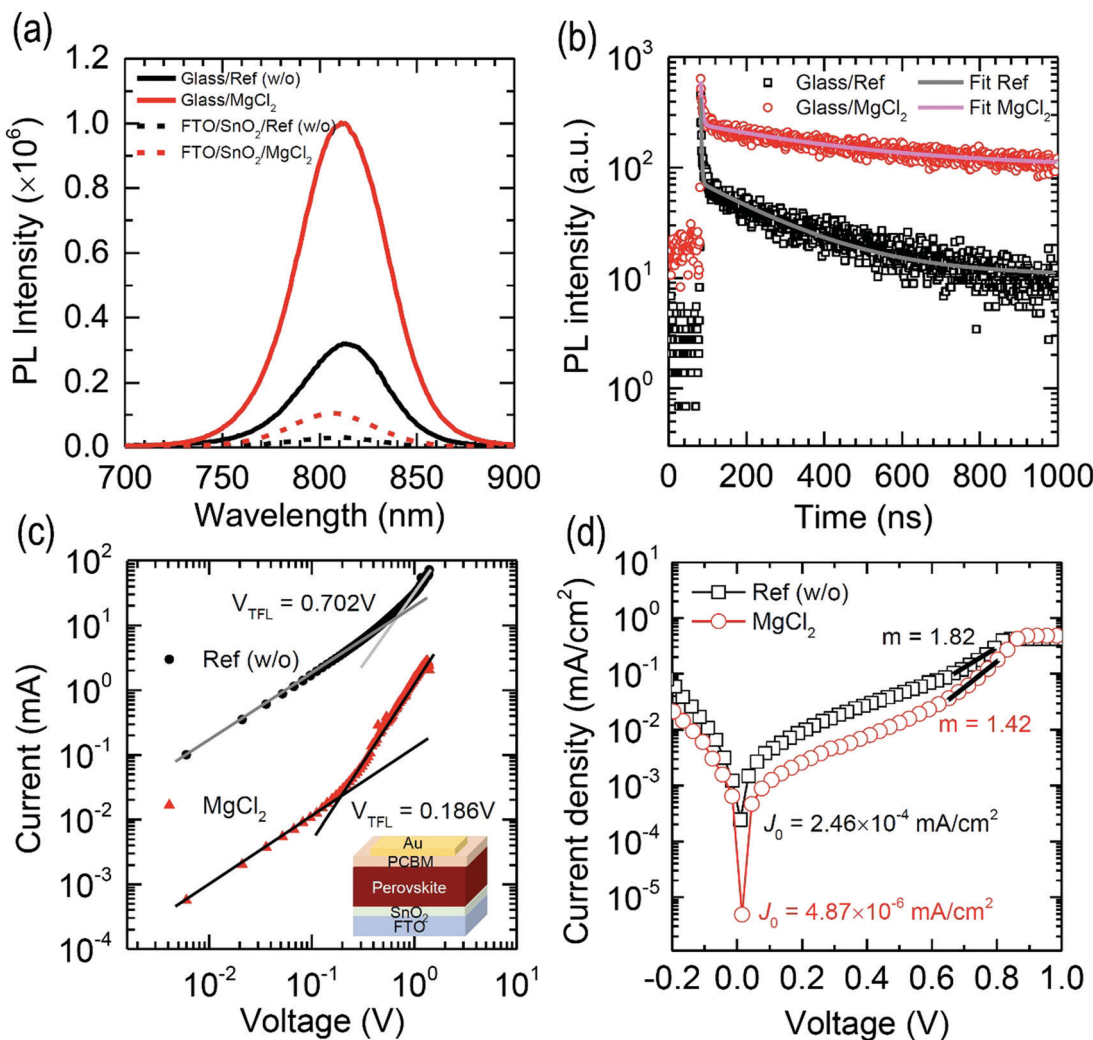


Fig. 7 (a) Steady-state photoluminescence (PL) of the FAPbI₃ film with and without MgCl₂ deposited on a glass substrate and SnO₂-coated FTO substrate. (b) Time-resolved PL (TRPL) for the FAPbI₃ film with and without MgCl₂ on a glass substrate. Dark current density (J)–voltage (V) curves for (c) the FTO/SnO₂/FAPbI₃ (with or without MgCl₂)/PCBM/Au electron-only device and (d) the full solar cell device.

Table 3 Parameters for fitting TRPL data with a bi-exponential decay equation of $f(t) = A_1 \exp(-t/\tau_1) + A_2 \exp(-t/\tau_2)$. Average lifetime (τ_{ave}) was calculated by the weighted average of $(A_1\tau_1^2 + A_2\tau_2^2)/(A_1\tau_1 + A_2\tau_2)$

Samples	A_1	τ_1 (ns)	A_2	τ_2 (ns)	τ_{ave} (ns)
Glass/perovskite w/o MgCl ₂	29111.5	1.9	65.0	201.2	40.1
Glass/perovskite w/MgCl ₂	4545.8	3.9	150.2	376.5	287.6

recombination pathway associated with τ_1 decreases or in other words is mostly suppressed by the additive. Since τ_1 is the one related to the surface defects, whereas τ_2 is linked to bulk traps,⁵² MgCl₂ appears to not only slow down the recombination process but suppress especially the presence of surface traps (*i.e.* the higher the number of surface traps, the larger the contribution (A_1)). As a result, average carrier lifetime (τ_{ave}) increases significantly from 40.1 ns to 287.6 ns after addition of MgCl₂. Trap density (n_t) is also evaluated from the space charge-limited current (SCLC) of a device with an electron-only configuration of FTO/SnO₂/perovskite/PCBM/Au⁵³ as shown in Fig. 7(c). n_t is

calculated based on the trap-filled-limit voltage (V_{TFL}) obtained from dark J – V curves in Fig. 7(c).¹⁵ V_{TFL} is estimated to be 0.702 V for the pristine FAPbI₃, which is significantly lowered to 0.186 V after the addition of MgCl₂. As a result, n_t decreases from 1.08×10^{16} cm^{−3}, which is consistent with the reported value,⁵⁴ to 3.19×10^{15} cm^{−3} after the addition of MgCl₂. The prolonged τ_{ave} is thus attributed to the decreased n_t . The reverse saturation current density (J_0) and the ideality factor (m) are also estimated from the full solar cell device structure in the dark. The dark J – V data shown in Fig. 7(d) result in $J_0 = 2.64 \times 10^{-4}$ mA cm^{−2} for the PSC employing the FAPbI₃ without additive, which is more than two orders of magnitude lowered after MgCl₂ ($J_0 = 4.87 \times 10^{-6}$ mA cm^{−2}). In addition, the addition of MgCl₂ lowers m from 1.82 to 1.42. The lower J_0 supports that the MgCl₂ additive in FAPbI₃ decreases shallow trap states. The reduced m is indicative of a suppression of the trap-assisted (mono molecular) recombination by the presence of MgCl₂ since the ideality factor correlates with the bimolecular band-to-band recombination ($m = 1$) and the Shockley–Read–Hall (SRH)

recombination ($m = 2$) in photoelectric devices.⁵⁵ The change in J_0 and m is also responsible for the improved V_{oc} and FF.^{56,57}

Efficiency and stability of PSCs employing the FAPbI₃ film with MgCl₂ additive

Fig. 8(a) shows the J – V curves for the best performing PSCs employing the FAPbI₃ films with and without 5 mol% MgCl₂. The relevant photovoltaic parameters obtained from RS and FS are listed in Table 4. The PCE estimated from RS is enhanced from 17.27% to 21.11% after addition of 5 mol% MgCl₂ in the FAPbI₃ precursor solution due to the increment of V_{oc} from 1.06 V to 1.15 V, FF from 0.73 to 0.79 and J_{sc} from 22.39 mA cm^{−2} to 23.33 mA cm^{−2}. The integrated J_{sc} s from the EQE data in Fig. 8(b) show a slight deviation from the measured J_{sc} values but the same tendency (20.07 mA cm^{−2} without additive vs. 22.32 mA cm^{−2} with MgCl₂ additive). It is found from the steady-state J_{sc} and PCE measured at the maximum power point (MPP) that J_{sc} and PCE remain almost unchanged after 1500 s (Fig. 8(c)). This indicates that the MgCl₂

Table 4 Photovoltaic parameters of the best performing PSCs employing FAPbI₃ with and without 5 mol% MgCl₂ additive. FS and RS stand for forward scan and reverse scan, respectively

		J_{sc} (mA cm ^{−2})	V_{oc} (V)	FF	PCE (%)
Ref (w/o)	FS	22.41	1.07	0.74	17.74
	RS	22.39	1.06	0.73	17.27
MgCl ₂ (5%)	FS	23.33	1.13	0.78	20.58
	RS	23.33	1.15	0.79	21.11

additive improves not only the efficiency but also the stability due to reduced bulk and surface defects simultaneously.

Conclusions

We have demonstrated that the addition of MgCl₂ in the FAPbI₃ precursor solution substantially improved the photovoltaic performance without altering the bandgap and lattice constant. It was also found that the concentration of the additive played an important role in determining the photovoltaic

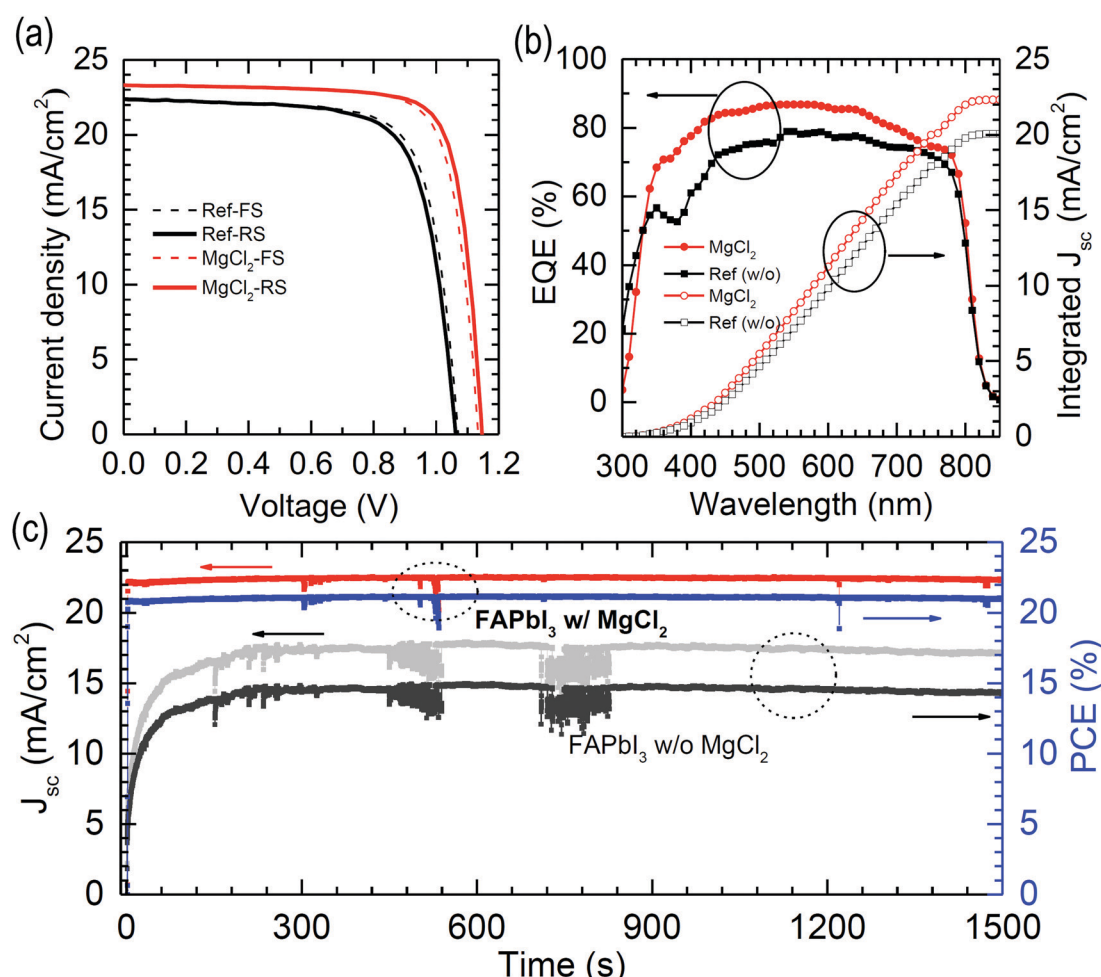


Fig. 8 (a) J – V curves and (b) external quantum efficiency (EQE) of PSCs employing FAPbI₃ with and without MgCl₂ additive. (c) Steady-state J_{sc} and PCE for the PSCs employing FAPbI₃ with and without the MgCl₂ additive, measured at the maximum power point (MPP) for 1500 s under continuous 1 sun illumination.

performance. CaCl_2 and BaCl_2 were found to increase the photovoltaic performance but the increment was marginal. For SrCl_2 , the addition of SrCl_2 showed a negative effect due to poor morphology and incomplete $\delta \rightarrow \alpha$ phase transition. Using a nominal concentration of 5 mol% of MgCl_2 , a photo-stable and 21.11% efficient PSC was achieved.

Experimental details

Materials

N,N-Dimethylformamide (DMF, 99.8%), dimethyl sulfoxide (DMSO, 99.9%), diethyl ether (99.7%), chlorobenzene (CB, 99.8%), formamidinium acetate (FAAc, 99%), lithium bis(trifluoromethane-sulfonyl)imide (LiTFSI, 99.8%), 4-*tert*-butylpyridine (*t*BP, 98%), acetonitrile (ACN, 99.999%), hydroiodic acid (HI, 57 wt% in water), magnesium chloride (MgCl_2 , 99.99%), calcium chloride (CaCl_2 , 99.9%), strontium chloride (SrCl_2 , 99.99%) and barium chloride (BaCl_2 , 99.999%) were purchased from Sigma-Aldrich. Aqueous colloidal tin(IV) oxide solution (SnO_2 , 15% in H_2O) was purchased from Alfa Aesar. 2,2',7,7'-tetrakis(*N,N'*-di-*p*-methoxyphenylamine)-9,9'-spirobifluorene (spiro-MeOTAD) was purchased from Share-Chem. Lead(II) iodide (PbI_2 , 95%) was purchased from Kanto Chemical Co., Inc. All the chemicals were used as-received without further purification. Fluorine doped tin oxide (FTO) glass (Pilkington, TEC-8, 8 Ωsq^{-1}) was used as a transparent electrode.

Synthesis of formamidinium iodide (FAI)

FAI was synthesized by reacting FAAC with HI. HI was slowly dropped into a round-bottom flask filled with FAAC, which was stirred for 2 h at 0 °C. The product was recovered by evaporating the solvent at 60 °C using a rotary evaporator, which was washed with diethyl ether and recrystallized from ethanol. Finally, the white precipitate was dried in a vacuum oven at 65 °C for 24 h and then stored in a glove box filled with argon prior to use.

Synthesis of FAPbI_3 powder

FAPbI_3 powder was synthesized by reacting FAI (2.236 g) with PbI_2 (4.61 g) (molar ratio FAI: PbI_2 = 1.3:1) in 60 ml ACN under stirring for 2 days at room temperature.²⁰ The product was dried in a vacuum oven for 2 days at room-temperature and then stored in a glove box filled with argon.

Device fabrication

FTO-coated glass was cleaned with solvents (water and ethanol), and was further treated with ultraviolet-ozone (UVO) for 40 min. A SnO_2 thin layer was prepared by spin-coating the diluted SnO_2 solution on the cleaned FTO substrate at 4000 rpm for 20 s and then annealed at 185 °C for 30 min. The SnO_2 -coated FTO substrate was treated with UVO for 20 min prior to deposition of the perovskite precursor. The perovskite precursor solution was prepared by dissolving the pre-synthesized FAPbI_3 powder (concentration was 1.4 M) in a mixed solvent of DMF and DMSO (DMF:DMSO = 8:1 v/v). To study the effect of the additives, a certain amount of additive (MgCl_2 (5%): 0.0033 g, CaCl_2 (1%): 0.0008 g, SrCl_2 (10%): 0.0111 g, and CaCl_2 (9%): 0.0131 g) was mixed with 0.4431 g of FAPbI_3 powder in 0.5 ml of DMF/DMSO mixed solvent, which was stirred for over 12 h. It should be noted that MgCl_2 itself was dissolved well in the mixed DMF/DMSO solvent but a precipitate was partially formed when it was mixed with FAPbI_3 . Thus filtration was required especially for the MgCl_2 case. For the perovskite deposition, the spin-coating condition was as follows. The precursor solution was filtered and 25 μl of precursor solution was spread on a SnO_2 /FTO substrate, which was spun at 1000 rpm for 5 s and 5000 rpm for 20 s. Diethyl ether (1 ml) was dripped 20 s after spinning. The as-spun film was annealed at 150 °C for 30 min. A spiro-MeOTAD hole transporting layer was formed on the perovskite film by spin coating 20 μl of the spiro-MeOTAD solution (72.3 mg of spiro-MeOTAD, 28.8 μl of *t*BP, and 17.5 μl of LiTFSI solution (520 mg LiTFSI in 1 ml ACN in 1 mL of CB)) at 4000 rpm for 20 s. On top of the spiro-MeOTAD layer, a *ca.* 65 nm-thick Au electrode was formed by a thermal evaporation method at an evaporation rate of 0.3 \AA s^{-1} under *ca.* 3.8×10^{-7} Torr.

(1%): 0.0008 g, SrCl_2 (10%): 0.0111 g, and CaCl_2 (9%): 0.0131 g) was mixed with 0.4431 g of FAPbI_3 powder in 0.5 ml of DMF/DMSO mixed solvent, which was stirred for over 12 h. It should be noted that MgCl_2 itself was dissolved well in the mixed DMF/DMSO solvent but a precipitate was partially formed when it was mixed with FAPbI_3 . Thus filtration was required especially for the MgCl_2 case. For the perovskite deposition, the spin-coating condition was as follows. The precursor solution was filtered and 25 μl of precursor solution was spread on a SnO_2 /FTO substrate, which was spun at 1000 rpm for 5 s and 5000 rpm for 20 s. Diethyl ether (1 ml) was dripped 20 s after spinning. The as-spun film was annealed at 150 °C for 30 min. A spiro-MeOTAD hole transporting layer was formed on the perovskite film by spin coating 20 μl of the spiro-MeOTAD solution (72.3 mg of spiro-MeOTAD, 28.8 μl of *t*BP, and 17.5 μl of LiTFSI solution (520 mg LiTFSI in 1 ml ACN in 1 mL of CB)) at 4000 rpm for 20 s. On top of the spiro-MeOTAD layer, a *ca.* 65 nm-thick Au electrode was formed by a thermal evaporation method at an evaporation rate of 0.3 \AA s^{-1} under *ca.* 3.8×10^{-7} Torr.

Characterization

Current density-voltage (*J-V*) curves were obtained by a solar simulator with a 450 W xenon lamp (Newport 6279 NS) and a Keithley 2400 source meter. The AM 1.5G one sun (100 mW cm^{-2}) was adjusted by the NREL-calibrated silicon reference solar cell with a KG-5 filter. The external quantum efficiency (EQE) was measured using an EQE system equipped with a 75 W xenon lamp (USHIO) as a white light source, where the monochromatic beam was generated by chopping the white light. Scanning electron microscopy (SEM) images were observed with field-emission scanning electron microscopy (JSM7000F). UV-vis spectra were recorded using a UV-vis spectrophotometer (Lambda 45, PerkinElmer). Steady-state photoluminescence (PL) and time-resolved photoluminescence (TRPL) spectra were measured using a fluorescence spectrometer (QuantaurusTau C11367-12, Hamamatsu) with excitation of a 464 nm laser (PLP-10, Hamamatsu) pulsed at a frequency of 10 MHz for steady-state PL and 200 kHz for TRPL. X-ray diffraction (XRD) patterns were obtained by the diffractometer (Rigaku Smart lab SE) with monochromatic $\text{Cu K}\alpha$ radiation ($\lambda = 1.54056 \text{\AA}$) at a scan rate of 4° min^{-1} . X-ray photoelectron spectroscopy (XPS) and ultraviolet photoelectron spectroscopy (UPS) measurements were carried out on an ESCALAB 250 XPS system (Thermo Fisher Scientific) with $\text{Al K}\alpha$ X-ray radiation (1486.6 eV) for XPS and He I (21.2 eV) for UPS.

Conflicts of interest

The authors declare no conflict of interest.

Acknowledgements

This work was supported by the National Research Foundation of Korea (NRF) grants funded by the Ministry of Science and ICT (MSIT) of Korea under contracts NRF-2012M3A6A7054861

(Global Frontier R&D Program on Center for Multiscale Energy System), NRF-2016M3D1A1027663 and NRF-2016M3D1A1027664 (Future Materials Discovery Program) and NRF-2015M1A2A2-053004 (Climate Change Management Program).

Notes and references

- 1 H.-S. Kim, C.-R. Lee, J.-H. Im, K.-B. Lee, T. Moehl, A. Marchioro, S.-J. Moon, R. Humphry-Baker, J.-H. Yum, J. E. Moser, M. Grätzel and N.-G. Park, Lead Iodide Perovskite Sensitized All-Solid-State Submicron Thin Film Mesoscopic Solar Cell with Efficiency Exceeding 9%, *Sci. Rep.*, 2012, **2**, 591.
- 2 A. Kojima, K. Teshima, Y. Shirai and T. Miyasaka, Organometal Halide Perovskites as Visible-Light Sensitizers for Photovoltaic Cells, *J. Am. Chem. Soc.*, 2009, **131**, 6050–6051.
- 3 J.-H. Im, C.-R. Lee, J.-W. Lee, S.-W. Park and N.-G. Park, 6.5% efficient perovskite quantum-dot-sensitized solar cell, *Nanoscale*, 2011, **3**, 4088–4093.
- 4 <https://www.nrel.gov/pv/cell-efficiency.html>, accessed on April 29, 2020.
- 5 W. A. Laban and L. Etgar, Depleted hole conductor-free lead halide iodide heterojunction solar cells, *Energy Environ. Sci.*, 2013, **6**, 3249–3253.
- 6 G. C. Xing, N. Mathews, S. Y. Sun, S. S. Lim, Y. M. Lam, M. Grätzel, S. Mhaisalkar and T. C. Sum, Long-Range Balanced Electron- and Hole-Transport Lengths in Organic-Inorganic $\text{CH}_3\text{NH}_3\text{PbI}_3$, *Science*, 2013, **342**, 344–347.
- 7 M. A. Green, A. Ho-Baillie and H. J. Snaith, The emergence of perovskite solar cells, *Nat. Photonics*, 2014, **8**, 506–514.
- 8 J.-W. Lee, D.-J. Seol, A.-N. Cho and N.-G. Park, High-Efficiency Perovskite Solar Cells Based on the Black Polymorph of $\text{HC}(\text{NH}_2)_2\text{PbI}_3$, *Adv. Mater.*, 2014, **26**, 4991–4998.
- 9 X. J. Zheng, C. C. Wu, S. K. Jha, Z. Li, K. Zhu and S. Priya, Improved Phase Stability of Formamidinium Lead Triiodide Perovskite by Strain Relaxation, *ACS Energy Lett.*, 2016, **1**, 1014–1020.
- 10 J.-W. Lee, D.-H. Kim, H.-S. Kim, S.-W. Seo, S. M. Cho and N.-G. Park, Formamidinium and Cesium Hybridization for Photo- and Moisture-Stable Perovskite Solar Cell, *Adv. Energy Mater.*, 2015, **5**, 1501310.
- 11 W. S. Yang, J. H. Noh, N. J. Jeon, Y. C. Kim, S. Ryu, J. Seo and S. I. Seok, High-performance photovoltaic perovskite layers fabricated through intramolecular exchange, *Science*, 2015, **348**, 1234–1237.
- 12 C. Mu, J. L. Pan, S. Q. Feng, Q. Li and D. S. Xu, Quantitative Doping of Chlorine in Formamidinium Lead Trihalide ($\text{FAPbI}_3(3-x)\text{Cl}(x)$) for Planar Heterojunction Perovskite Solar Cells, *Adv. Energy Mater.*, 2017, **7**, 1601297.
- 13 J.-W. Lee and N.-G. Park, Chemical Approaches for Stabilizing Perovskite Solar Cells, *Adv. Energy Mater.*, 2020, **10**, 1903249.
- 14 N.-G. Park and K. Zhu, Scalable fabrication and coating methods for perovskite solar cells and solar modules, *Nat. Rev. Mater.*, 2020, **5**, 333–350.
- 15 S.-G. Kim, J. Chen, J.-Y. Seo, D.-H. Kang and N.-G. Park, Rear-Surface Passivation by Melaminium Iodide Additive for Stable and Hysteresis-less Perovskite Solar Cells, *ACS Appl. Mater. Interfaces*, 2018, **10**, 25372–25383.
- 16 M. Mateen, Z. Arain, Y. Yang, X. Liu, S. Ma, C. Liu, Y. Ding, X. Ding, M. Cai and S. Dai, MACl-Induced Intermediate Engineering for High-Performance Mixed-Cation Perovskite Solar Cells, *ACS Appl. Mater. Interfaces*, 2020, **12**, 10535–10543.
- 17 M. Kim, G.-H. Kim, T. K. Lee, I. W. Choi, H. W. Choi, Y. Jo, Y. J. Yoon, J. W. Kim, J. Lee, D. Huh, H. Lee, S. K. Kwak, J. Y. Kim and D. S. Kim, Methylammonium Chloride Induces Intermediate Phase Stabilization for Efficient Perovskite Solar Cells, *Joule*, 2019, **3**, 2179–2192.
- 18 G. Yang, H. Zhang, G. Li and G. Fang, Stabilizer-assisted growth of formamidinium-based perovskites for highly efficient and stable planar solar cells with over 22% efficiency, *Nano Energy*, 2019, **63**, 103835.
- 19 B. Lee, T. Hwang, S. Lee, B. Shin and B. Park, Microstructural Evolution of Hybrid Perovskites Promoted by Chlorine and its Impact on the Performance of Solar Cell, *Sci. Rep.*, 2019, **9**, 4803.
- 20 Y. Zhang, S. Seo, S. Y. Lim, Y. Kim, S.-G. Kim, D.-K. Lee, S.-H. Lee, H. Shin, H. Cheong and N.-G. Park, Achieving Reproducible and High-Efficiency (> 21%) Perovskite Solar Cells with a Presynthesized FAPbI_3 Powder, *ACS Energy Lett.*, 2020, **5**, 360–366.
- 21 G. S. Shin, S.-G. Kim, Y. Zhang and N.-G. Park, A Correlation between Iodoplumbate and Photovoltaic Performance of Perovskite Solar Cells Observed by Precursor Solution Aging, *Small Methods*, 2020, **4**, 1900398.
- 22 Y. Deng, C. H. V. Brackley, X. Dai, J. Zhao, B. Chen and J. Huang, Tailoring solvent coordination for high-speed, room-temperature blading of perovskite photovoltaic films, *Sci. Adv.*, 2019, **5**, eaax7537.
- 23 N. Ahn, D.-Y. Son, I.-H. Jang, S. M. Kang, M. Choi and N.-G. Park, Highly Reproducible Perovskite Solar Cells with Average Efficiency of 18.3% and Best Efficiency of 19.7% Fabricated via Lewis Base Adduct of Lead(II) Iodide, *J. Am. Chem. Soc.*, 2015, **137**, 8696–8699.
- 24 S.-H. Chan, M.-C. Wu, K.-M. Lee, W.-C. Chen, T.-H. Lina and W.-F. Su, Enhancing perovskite solar cell performance and stability by doping barium in methylammonium lead halide, *J. Mater. Chem. A*, 2017, **5**, 18044–18052.
- 25 M.-C. Wu, T.-H. Lin, S.-H. Chan, Y.-H. Liao and Y.-H. Chang, Enhanced Photovoltaic Performance of Perovskite Solar Cells by Tuning Alkaline Earth Metal-Doped Perovskite-Structured Absorber and Metal-Doped TiO_2 Hole Blocking Layer, *ACS Appl. Energy Mater.*, 2018, **1**, 4849–4859.
- 26 H. Zhang, H. Wang, S. T. Williams, D. Xiong, W. Zhang, C.-C. Chueh, W. Chen and A. K.-Y. Jen, SrCl_2 Derived Perovskite Facilitating a High Efficiency of 16% in Hole-Conductor-Free Fully Printable Mesoscopic Perovskite Solar Cells, *Adv. Mater.*, 2017, **29**, 1606608.
- 27 C. F. J. Lau, M. Zhang, X. Deng, J. Zheng, J. Bing, Q. Ma, J. Kim, L. Hu, M. A. Green, S. Huang and A. Ho-Baillie, Strontium-Doped Low-Temperature-Processed CsPbI_2Br Perovskite Solar Cells, *ACS Energy Lett.*, 2017, **2**, 2319–2325.
- 28 F. Yang, M. A. Kamarudin, G. Kapil, D. Hirotani, P. Zhang, C. H. Ng, T. Ma and S. Hayase, Magnesium-Doped MAPbI_3

Perovskite Layers for Enhanced Photovoltaic Performance in Humid Air Atmosphere, *ACS Appl. Mater. Interfaces*, 2018, **10**, 24543–24548.

29 R. Chen, D. Hou, C. Lu, J. Zhang, P. Liu, H. Tian, Z. Zeng, Q. Xiong, Z. Hu, Y. Zhu and L. Han, Zinc ion as Effective Film Morphology Controller in Perovskite Solar Cells, *Sustainable Energy Fuels*, 2018, **2**, 1093–1100.

30 N. Guijarro, M. S. Prévot, X. Yu, X. A. Jeanbourquin, P. Bornoz, W. Bourée, M. Johnson, F. L. Formal and K. Sivula, A Bottom-Up Approach toward All-Solution-Processed High-Efficiency Cu(In,Ga)S₂ Photocathodes for Solar Water Splitting, *Adv. Energy Mater.*, 2016, **6**, 1501949.

31 G. S. Shin, Y. Zhang and N.-G. Park, Stability of Precursor Solution for Perovskite Solar Cell: Mixture (FAI + PbI₂) versus Synthetic FAPbI₃ Crystal, *ACS Appl. Mater. Interfaces*, 2020, **12**, 15167–15174.

32 H. Zhou, Q. Chen, G. Li, S. Luo, T.-B. Song, H.-S. Duan, Z. Hong, J. You, Y. Liu and Y. Yang, Interface engineering of highly efficient perovskite solar cells, *Science*, 2014, **345**, 542–546.

33 D.-Y. Son, J.-W. Lee, Y. J. Choi, I.-H. Jang, S. Lee, P. J. Yoo, H. Shin, N. Ahn, M. Choi, D. Kim and N.-G. Park, Self-formed grain boundary healing layer for highly efficient CH₃NH₃PbI₃ perovskite solar cells, *Nat. Energy*, 2016, **1**, 1–8.

34 L. K. Ono, S. (Frank) Liu and Y. Qi, Reducing Detrimental Defects for High-Performance Metal Halide Perovskite Solar Cells, *Angew. Chem. Int. Ed.*, 2020, **59**, 6676–6698.

35 J. Chen, J.-Y. Seo and N.-G. Park, Simultaneous Improvement of Photovoltaic Performance and Stability by In Situ Formation of 2D Perovskite at (FAPbI₃)_{0.88}(CsPbBr₃)_{0.12}/CuSCN Interface, *Adv. Energy Mater.*, 2018, **8**, 1702714.

36 M. Kot, M. Vorokhta, Z. Wang, H. J. Snaith, D. Schmeißer and J. I. Fleg, Thermal stability of CH₃NH₃PbI_xCl_{3-x} versus [HC(NH₂)₂]_{0.83}Cs_{0.17}PbI_{2.7}Br_{0.3} perovskite films by X-ray photoelectron spectroscopy, *Appl. Surf. Sci.*, 2020, **513**, 145596.

37 J. Chen, S.-G. Kim, X. Ren, H. S. Jung and N.-G. Park, Effect of bidentate and tridentate additives on the photovoltaic performance and stability of perovskite solar cells, *J. Mater. Chem. A*, 2019, **7**, 4977–4987.

38 H.-L. Hsu, H.-T. Hsiao, T.-Y. Juang, B.-H. Jiang, S.-C. Chen, R.-J. Jeng and C.-P. Chen, Perovskite Solar Cells: Carbon Nanodot Additives Realize High-Performance Air-Stable p-i-n Perovskite Solar Cells Providing Efficiencies of up to 20.2%, *Adv. Energy Mater.*, 2018, **8**, 1802323.

39 J. Li, T. Jiu, S. Chen, L. Liu, Q. Yao, F. Bi, C. Zhao, Z. Wang, M. Zhao and G. Zhang, Graphdiyne as a Host Active Material for Perovskite Solar Cell Application, *Nano Lett.*, 2018, **18**, 6941–6947.

40 K. Fajans, Struktur und Deformation der Elektronenhüllen in ihrer Bedeutung für die chemischen und optischen Eigenschaften anorganischer Verbindungen, *Naturwissenschaften*, 1923, **11**, 165–172.

41 S. Wang, H. Cao, X. Liu, Y. Liu, T. Tao, J. Sun and M. Zhang, Strontium Chloride Passivated Perovskite Thin Films for Efficient Solar Cells with Power Conversion Efficiency over 21% and Superior Stability, *ACS Appl. Mater. Interfaces*, 2020, **12**, 3661–3669.

42 M. Pazoki, T. J. Jacobsson, A. Hagfeldt, G. Boschloo and T. Edvinsson, Effect of metal cation replacement on the electronic structure of metalorganic halide perovskites: Replacement of lead with alkaline-earth metals, *Phys. Rev. B*, 2016, **93**, 144105.

43 J. Navas, A. Sánchez-Coronilla, J. J. Gallardo, N. C. Hernández, J. C. Piñero, R. Alcántara, C. Fernández-Lorenzo, D. M. D. I. Santos, T. Aguilar and J. Martín-Calleja, New insights into organic-inorganic hybrid perovskite CH₃NH₃PbI₃ nanoparticles. An experimental and theoretical study of doping in Pb²⁺ sites with Sn²⁺, Sr²⁺, Cd²⁺ and Ca²⁺, *Nanoscale*, 2015, **7**, 6216–6229.

44 T. J. Jacobsson, M. Pazoki, A. Hagfeldt and T. Edvinsson, Goldschmidt's Rules and Strontium Replacement in Lead Halogen Perovskite Solar Cells: Theory and Preliminary Experiments on CH₃NH₃SnI₃, *J. Phys. Chem. C*, 2015, **119**, 25673–25683.

45 C. F. J. Lau, X. Deng, J. Zheng, J. Kim, Z. Zhang, M. Zhang, J. Bing, B. Wilkinson, L. Hu, R. Patterson, S. Huang and A. Ho-Baillie, Enhanced performance via partial lead replacement with calcium for a CsPbI₃ perovskite solar cell exceeding 13% power conversion efficiency, *J. Mater. Chem. A*, 2018, **6**, 5580–5586.

46 B. Philippe, T. J. Jacobsson, J.-P. Correa-Baena, N. K. Jena, A. Banerjee, S. Chakraborty, U. B. Cappel, R. Ahuja, A. Hagfeldt, M. Odelius and H. Rensmo, Valence Level Character in a Mixed Perovskite Material and Determination of the Valence Band Maximum from Photoelectron Spectroscopy: Variation with Photon Energy, *J. Phys. Chem. C*, 2017, **121**, 26655–26666.

47 J. Endres, D. A. Egger, M. Kulbak, R. A. Kerner, L. Zhao, S. H. Silver, G. Hodes, B. P. Rand, D. Cahen, L. Kronik and A. Kahn, Valence and Conduction Band Densities of States of Metal Halide Perovskites: A Combined Experimental-Theoretical Study, *J. Phys. Chem. Lett.*, 2016, **7**, 2722–2729.

48 S. Tao, I. Schmidt, G. Brocks, J. Jiang, I. Tranca, K. Meerholz and S. Olthof, Absolute energy level positions in tin and lead-based halide perovskites, *Nat. Commun.*, 2019, **10**, 1–10.

49 C. Lu, J. Zhang, D. Hou, X. Gan, H. Sun, Z. Zeng, R. Chen, H. Tian, Q. Xiong, Y. Zhang, Y. Li and Y. Zhu, Calcium doped MAPbI₃ with better energy state alignment in perovskite solar cells, *Appl. Phys. Lett.*, 2018, **112**, 193901.

50 W.-J. Yin, H. Chen, T. Shi, S.-H. Wei and Y. Yan, Origin of High Electronic Quality in Structurally Disordered CH₃NH₃PbI₃ and the Passivation Effect of Cl and O at Grain Boundaries, *Adv. Electron. Mater.*, 2015, **1**, 1500044.

51 N. Phung, R. Félix, D. Meggiolaro, A. Al-Ashouri, G. S. E. Silva, C. Hartmann, J. Hidalgo, H. Köbler, E. Mosconi, B. Lai, R. Gunder, M. Li, K.-L. Wang, Z.-K. Wang, K. Nie, E. Handick, R. G. Wilks, J. A. Marquez, B. Rech, T. Unold, J.-P. Correa-Baena, S. Albrecht, F. D. Angelis, M. Bär and A. Abate, The Doping Mechanism of Halide Perovskite Unveiled by Alkaline Earth Metals, *J. Am. Chem. Soc.*, 2020, **142**, 2364–2374.

52 Y. Zhang, S.-G. Kim, D. Lee, H. Shin and N.-G. Park, Bifacial stamping for high efficiency perovskite solar cells, *Energy Environ. Sci.*, 2019, **12**, 308–321.

53 D. Yang, X. Zhou, R. Yang, Z. Yang, W. Yu, X. Wang, C. Li, S. (Frank) Liu and R. P. H. Chang, Surface optimization to

eliminate hysteresis for record efficiency planar perovskite solar cells, *Energy Environ. Sci.*, 2016, **9**, 3071–3078.

54 D.-Y. Son, S.-G. Kim, J.-Y. Seo, S.-H. Lee, H. Shin, D. Lee and N.-G. Park, Universal approach toward hysteresis-free perovskite solar cell via defect engineering, *J. Am. Chem. Soc.*, 2018, **140**, 1358–1364.

55 T. He, S. Li, Y. Jiang, C. Qin, M. Cui, L. Qiao, H. Xu, J. Yang, R. Long, H. Wang and M. Yuan, Reduced-dimensional perovskite photovoltaics with homogeneous energy landscape, *Nat. Commun.*, 2020, **11**, 1672.

56 W. Tress, Perovskite Solar Cells on the Way to Their Radiative Efficiency Limit-Insights Into a Success Story of High Open-Circuit Voltage and Low Recombination, *Adv. Energy Mater.*, 2017, **7**, 1602358.

57 N.-G. Park and H. Segawa, Research Direction toward Theoretical Efficiency in Perovskite Solar Cells, *ACS Photonics*, 2018, **5**, 2970–2977.